Author/s:
Tang, J;Tang, J;Mayyas, M;Ghasemian, MB;Sun, J;Rahim, MA;Yang, J;Han, J;Lawes, DJ;Jalili, R;Daeneke, T;Saborio, MG;Cao, Z;Echeverria, CA;Allioux, FM;Zavabeti, A;Hamilton, J;Mitchell, V;O'Mullane, AP;Kaner, RB;Esrafilzadeh, D;Dickey, MD;Kalantar-Zadeh, K

Title:
Liquid-Metal-Enabled Mechanical-Energy-Induced CO2 Conversion

Date:
2022-01-01

Citation:
Tang, J., Tang, J., Mayyas, M., Ghasemian, M. B., Sun, J., Rahim, M. A., Yang, J., Han, J., Lawes, D. J., Jalili, R., Daeneke, T., Saborio, M. G., Cao, Z., Echeverria, C. A., Allioux, F. M., Zavabeti, A., Hamilton, J., Mitchell, V., O'Mullane, A. P. ,... Kalantar-Zadeh, K. (2022). Liquid-Metal-Enabled Mechanical-Energy-Induced CO2 Conversion. Advanced Materials, 34 (1), https://doi.org/10.1002/adma.202105789.

Liquid metal-enabled mechanical energy-induced CO_2 conversion

Junma Tang, Jianbo Tang, Mohannad Mayyas, Mohammad B. Ghasemian, Jing Sun, Md Arifur Rahim, Jiong Yang, Jialuo Han, Douglas J. Lawes, Rouhollah Jalili, Torben Daeneke, Zhenbang Cao, Claudia A. Echeverria, Francois-Marie Allioux, Ali Zavabeti, Jessica Hamilton, Valerie Mitchell, Anthony P. O'Mullane, Richard B. Kaner, Dorna Esrafilzadeh*, Michael D. Dickey, Kourosh Kalantar-Zadeh**

J. Tang, Dr. J. Tang, Dr. M. Mayyas, Dr. M. B. Ghasemian, J. Sun, Dr. M. A. Rahim, Dr. J. Yang, J. Han, Dr. R. Jalili, Dr. Z. Cao, Dr. C. A. Echeverria, Dr. F. M. Allioux, Pro. K. Kalantar-Zadeh

School of Chemical Engineering

University of New South Wales (UNSW)

Sydney 2052, Australia

E-mail: k.kalantar-zadeh@unsw.edu.au

Dr. D. J. Lawes

Mark Wainwright Analytical Centre

University of New South Wales (UNSW)

Sydney 2052, Australia

Dr. T. Daeneke

School of Engineering

Royal Melbourne Institute of Technology (RMIT)

Melbourne 3001, Australia

This is the author manuscript accepted for publication and has undergone full peer review but has not been through the copyediting, typesetting, pagination and proofreading process, which may lead to differences between this version and the Version of Record. Please cite this article as doi: 10.1002/adma.202105789.

Dr. A. Zavabeti

Department of Chemical Engineering

The University of Melbourne

Parkville, VIC 3010, Australia

Dr. J. Hamilton, Dr. V. Mitchell

Australian Synchrotron, ANSTO

Clayton, VIC 3168, Australia

Pro. A. P. O'Mullane

School of Chemistry and Physics

Queensland University of Technology (QUT)

Brisbane, QLD 4001, Australia

Pro. R. B. Kaner

Department of Chemistry and Biochemistry and California NanoSystems Institute

University of California

Los Angeles, California 90095, United States

Pro. R. B. Kaner

Department of Material Science and Engineering,

University of California

Los Angeles, California 90095, United States

Dr. D. Esrafilzadeh

Graduate School of Biomedical Engineering

University of New South Wales (UNSW)

Sydney 2052, Australia

Pro. M. D. Dickey

Department of Chemical and Biomolecular Engineering

North Carolina State University

Raleigh, North Carolina 27695, United States

Keywords: CO_2 conversion, liquid metal, mechanical energy, triboelectrochemical reactions

We report a green carbon capture and conversion technology offering scalability and economic viability for mitigating CO_2 emissions. The technology uses suspensions of gallium liquid metal to reduce CO_2 into carbonaceous solid products and O_2 at near room temperature. The nonpolar nature of the liquid gallium interface allows the solid products to instantaneously exfoliate, hence keeping active sites accessible. The solid co-contributor of silver-gallium rods ensures a cyclic sustainable process. The overall process relies on mechanical energy as the input, which drives nano dimensional triboelectrochemical reactions. When a gallium/silver fluoride mix at 7:1 mass ratio is employed to create the reaction material, 92% efficiency was obtained at the remarkably low input energy of 230 kW·h for the capture and conversion of a tonne of CO_2. This green technology presents an economical solution for CO_2 emissions.

1. Introduction

Innovative technologies are urgently demanded for capturing and converting CO_2 into value-added species, at low input energy, to mitigate the negative effects of this greenhouse gas and support a sustainable carbon cycle.[1, 2] Activating CO_2 into $CO_2^{\bullet-}$ radicals or other intermediates is a crucial step for CO_2 conversion, while the inertness of CO_2 molecules imposes a significant challenge.[3] To this end, external energy is required, and catalytic systems are commonly engaged to lower the energy barrier for CO_2 converting. The choices of both the applied energy and functional materials, and how they are pooled together for CO_2 conversion govern the efficiency balances. To date, light and electricity have been extensively used as the triggering energies together with many well-known catalytic systems.[4-8] However, in general, the existing electro- or photo- empowered CO_2 reduction systems suffer from sluggish reaction rates and high energy consumption. Additionally, there has also been no magical definitive catalyst, that could synergistically operate with these energy types to carry out the conversion at low costs and high efficiencies.

Mechanical energy is easy to generate and often a waste source of energy. Except for organic synthesis and polymerisation,[9, 10] mechanical energy has received little attention in catalytic systems[11] and has not yet been utilised for CO_2 reduction. In conductive particles suspensions, the introduction of mechanical stimuli can generate triboelectrification, as a result of the frictional contact in the presence of dielectric materials.[12]

Solid metallic catalysts have exhibited excellent performance for electrocatalytic or photocatalytic CO_2 reduction.[13-15] However, the active sites of solid metallic catalysts can deteriorate under intense mechanical stimuli and/or can be deactivated when carbonaceous materials adhere onto the catalytic sites during CO_2 reduction. In principle, the use of liquid metals, and specific solid structures, can solve these problems. Gallium (Ga)-based liquid metals have shown intriguing

properties for catalysis, including tunability by the incorporation of other elements, and remarkable resistance to coking[16-19] and also excellent mechanical tolerance. Additionally, it is known that Ga(0) can be oxidized to Ga^+ in the presence of organic materials.[20] In this work, we explore whether the same effect can also apply to CO_2 and whether we can find a process to reduce Ga^+ back to Ga(0) in a closed cycle stimulated by mechanical agitation. We envision that by employing liquid metal mixes of Ga and a compound of Ag, a closed cyclic catalytic system can be developed. This system can then covert CO_2 into value-added species in the reversible Ga-Ga^+ cycle, which will be fully explored.

2. Results and Discussion

2.1. Assessment of CO_2 conversion for various scenarios

We exploited a suspension of Ga and Ag(I) salt mixes as the precursors of the co-catalysts and ultrasound was initially employed to stimulate the CO_2 reduction. Dimethylformamide (DMF), with good stability during mechanical agitation and high CO_2 solubility of 0.14 M at 40 °C (to assure the liquid state of Ga), was chosen as the solvent.[21] We observed that during the reaction, the CO_2 molecules near the interface of the suspended particles were reduced to form carbonaceous sheets in a process that will be detailed later.

The best outcomes were obtained when Ga and AgF were mixed in a DMF solution which also contained 0.10 M HCl to remove the native oxide on the surface of Ga. Ga and AgF were sonicated together (**Figure 1**a - using a probe sonicator for 30 min) to generate sub-micron Ga droplets of 230 nm median diameters and $Ag_{0.72}Ga_{0.28}$ rods of micron/sub-micron lengths and median diameters of 160 nm (Figure 1b and Figure S1, Supporting Information). The characterisation outcomes revealing the elemental composition will be presented in a later section.

In the reactor, CO_2 was bubbled into DMF through a diffuser to facilitate its dissolving process (Figure 1c). The dissolved CO_2 is reduced to solid carbonaceous materials at the interface of the Ga droplets. The mechanically enforced CO_2 conversion can be scaled up using a variety of mechanical sources that produce frictional contact. To examine this prospect, CO_2 conversion by an overhead mixer was also performed and validated (Figure 1d).

Due to the ultra-smooth nature of the liquid metal droplets, the produced carbonaceous materials on the surface are in the form of sheets.[16, 22] These low dimensional sheets, on the non-polarized liquid metal surface, are exfoliated during mechanical stimulation (Figure 1e).[16, 22] Most importantly, the carbon sheets migrate to the top of the reactor and can be isolated due to the density difference with reference to that of metallic components (Figure 1c,d).

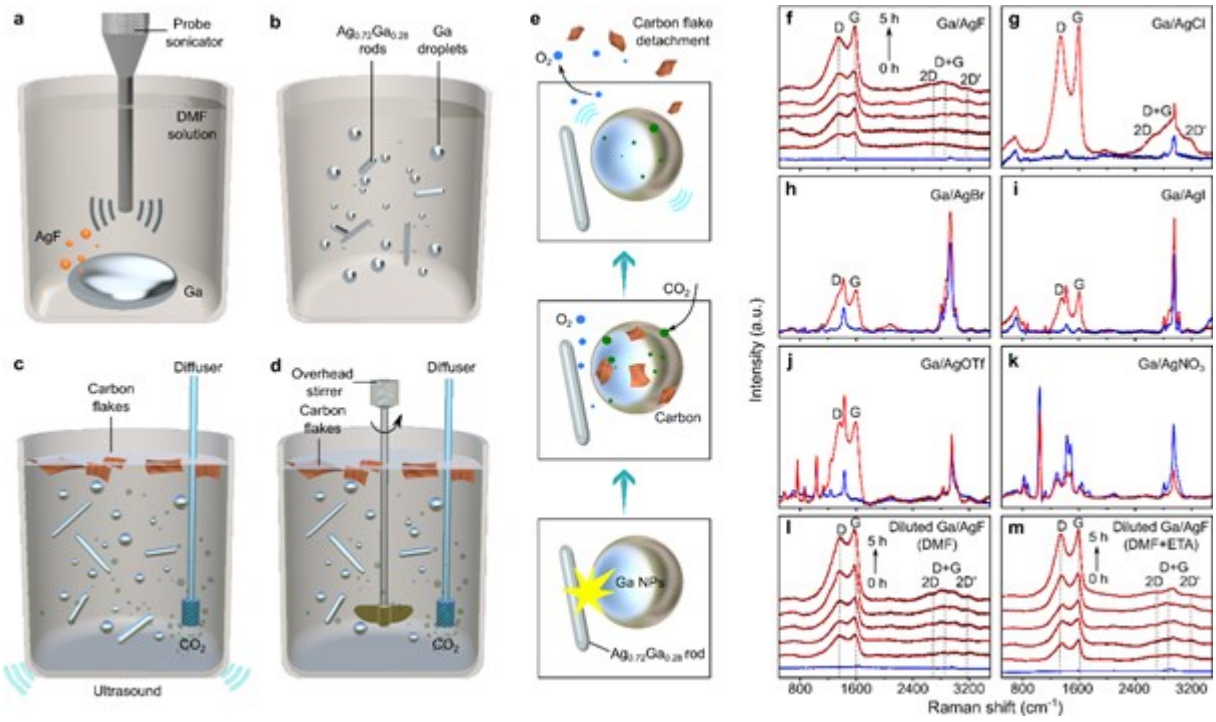

Figure 1. Schematics and Raman spectra of solid carbon produced from CO_2 using liquid metal. a-d) Schematic illustrations for the preparation of a suspension of catalyst (a,b) and the CO_2 reduction process using different mechanical energy inputs (c,d). e) Schematic illustration of the CO_2 conversion process. The formation/detachment of the carbon flakes and the generation/escape of

O_2 are indicated. f-k) Raman spectra of the samples obtained from the reaction mixes of Ga with different silver salts as precursors in DMF: AgF (f, versus time), AgCl (g), AgBr (h), AgI (i), AgOTf (j) and $AgNO_3$ (k). The D and G bands at 1350 and 1600 cm^{-1}, respectively, emerged after the reactions occur. l,m) Raman spectra (versus time) from the surface of mixtures from the 10-times diluted reaction system (Ga and AgF mix) by employing DMF (l) and DMF+ETA (m) as the reaction solutions. The blue and red curves in f-m are Raman spectra for the samples before and after reaction, respectively.

The qualitative and quantitative analyses of the production of carbon, when the Ga/AgF (7.0 to 1.0 mass ratio) suspension in DMF is utilised in a 20 mL reactor, are presented in Figure 1f and Figure S2. The 7.0 to 1.0 mass ratio and the reaction temperature were chosen according to previously optimised data for C-C bond formation reactions.[20] Additionally, the performance of the system formed by direct alloying of Ga with silver (50 to 1.0 or 20 to 1.0 mass ratio of Ga/Ag, Figure S3e,f, Supporting Information) and different silver salts (Figure 1g-k), including AgCl, AgBr, AgI, AgOTf, $AgNO_3$ (also 7.0 to 1.0 mass ratio) were compared. The homogeneous mixture (20 µL) was drop-casted onto a glass substrate and dried for Raman analysis, with the whole drop-cast region included during the Raman spectroscopy measurement (Figure S3a-d, Supporting Information). The changes in the intensity of the carbon D and G bands at 1350 and 1600 cm^{-1}, respectively, were employed to obtain the overall picture. Thermal gravimetric analyses (TGA) and gas chromatography (GC) were also conducted for comparative quantitative assessment of the solid carbon and gaseous products (Table S1, Supporting Information).

For the Ga/AgF system that exhibited the best performance, the production of carbon was observed in < 1 hour of reaction (Figure 1f) and increased continuously over time according to TGA. The TGA showed that 4.95 mg of carbonaceous materials were produced per hour in a 20 mL reactor at a CO_2 flow rate of ~10 sccm (0.027 mol h^{-1}) (Figure S2, Supporting Information). In comparison, the AgCl, AgBr, AgI, and AgOTf mixes also presented CO_2 conversion capability, but they were not as efficient as the AgF system (Figure 1g-j, for brevity only Raman spectra are shown and not TGA). With no

emerging D and G bands after 5 hours of reaction (Figure 1k and Figure S3e,f, Supporting Information), Ga/$AgNO_3$ and Ga-Ag alloys were found to be ineffective for CO_2 reduction. The reason for these different conversion activities will be discussed later.

To verify that the CO_2 reduction relies on the synergism of Ga and AgF, experiments were conducted by employing Ga and AgF separately (Figure S3g,h, Supporting Information), both of which resulted in undetectable carbon production. Also, the $Ag_{0.72}Ga_{0.28}$ rods alone could not achieve CO_2 conversion (Figure S4, Supporting Information). We note that our attempts with other types of salts (e.g. KCl and NaCl) showed no carbon formation, indicating the crucial role of the chosen silver salt (AgF) (Figure S3i,j, Supporting Information). Controlled N_2 bubbling also did not show any formation of carbonaceous products (Figure S3k, Supporting Information).

We explored the minimum co-catalyst mass required in the system to maintain the efficiency of CO_2 conversion. Diluting the catalyst by 10 times offered nearly the same conversion efficiency, still achieving an equivalent production of 4.75 mg of carbonaceous materials per hour at ~10 sccm CO_2 bubbling rate (Figure 1l and Figure S2, Supporting Information), whereas the output was dramatically reduced for dilutions of 50 or 100 times (Figure S3l,m, Supporting Information. TGA profiles are not shown for brevity).

The amount of CO_2 dissolved in solution significantly influenced the efficiency of CO_2 conversion. Ethanolamine (ETA) is a suitable choice for increasing this amount since CO_2 solubility is 5.6 M in pure ETA[23] in comparison to 0.14 M in DMF at 40 °C. With the addition of 10 vol% ETA in DMF (referred to as DMF+ETA hereafter), CO_2 was continuously reduced with a higher efficiency, producing 7.95 mg of carbonaceous materials per hour in the same reactor at ~10 sccm CO_2 bubbling rate (Figure 1m and Figure S2, Supporting Information). Interestingly, 22.2 cm^3 (9.52×10^{-4} mol) CO was also produced in one hour (Figure S5, Supporting Information). In contrast, when DMSO or H_2O

were used, the efficiency was very low and carbon products could not be quantified by TGA, owing to their limited CO_2 solubility (Figure S3n,o, Supporting Information).

2.2. Carbonaceous materials characterisation

Carbonaceous materials produced from CO_2 were isolated for further characterisation. Scanning electron microscopy (SEM) and energy-dispersive X-ray spectroscopy (EDS) analysis (**Figure 2**a and Figure S6a, Supporting Information) of the isolated carbonaceous materials reveal that the solid product consists of carbon and oxygen before any secondary washing, with trace quantities of the metallic species that can be easily removed. Fourier transform infrared (FTIR) spectroscopy (Figure S6b,c, Supporting Information) further confirms that the carbonaceous materials are primarily comprised of C=C and C-O bonds.[17] Based on X-ray photoelectron spectroscopy (XPS) analysis, the C1s region of the carbonaceous materials shows characteristic peaks of sp^2 carbon and C-O bonding, at 284.2 and 286.1 eV, respectively (Figure S6d, Supporting Information).[24] The presence of C-O bonds is validated from the O1s XPS region of the sample (Figure S6e, Supporting Information). Transmission electron microscopy (TEM) and selected area electron diffraction (SAED) images demonstrate that part of the carbonaceous material is akin to that of slightly crystalline graphene oxide (Figure 2b), and a certain proportion of the product exists in the amorphous state (Figure S6f, Supporting Information).

2.3. Efficiency and energy requirement for CO_2 conversion

The CO_2 conversion efficiencies under different configurations were determined using TGA and GC measurements as summarised in Table S1 (see Supporting Information). The conversion efficiency is

defined as (captured and reduced CO_2/total input CO_2)×100%, which are all obtained from the optimum mix of Ga/AgF (to be explained further in the next section).

In the small-volume reactor of 20 mL and height of 4.5 cm, which was used as the characterisation unit in the previous sections, the conversion efficiencies are 1.5% and 6.2%, for DMF and DMF+ETA cases, respectively (Figure 2c). To demonstrate the scalability, we increased the dimensions of the reactor (Figure 2d). When the height of the reactor was increased to 40 cm for only DMF solvent (volume of 500 mL), 27% of the input CO_2 at the flow rate of ~8.6 sccm (0.0232 mol h^{-1}) could be continuously captured and converted (Figure 2c). Thus, when the total height of the reactor would be 148 cm, the CO_2 conversion could reach the full capacity.

The height of the reactor for near-full conversion could be significantly decreased when DMF+ETA was used as the solvent as this combination could significantly increase the CO_2 solubility. The conversion efficiency reached the unprecedented value of 92% (at the flow of ~8.0 sccm CO_2, 0.0216 mol h^{-1}) in this case for a reactor as small as 27 cm in height and 330 mL in volume (Figure 2c, see Figure S7 for the photo of the set-up and Supplementary discussion for the corresponding turnover number, Supporting Information). The amount of produced O_2 and carbonaceous materials (highly oxidised carbon), under different conditions, are presented in Figure S8 and Table S1 in Supporting Information. To assess the stability and durability of the system, the reaction was conducted continuously for a period of over 100 hours. As presented in the Figure S9 to S11 and Supplementary discussion in Supporting Information, there is no deterioration of the performance or change of the catalytic materials and solvent in the reactor.

According to these measurements, the total energies required for converting 1.0 tonne of CO_2, for DMF and DMF+ETA cases, are obtained as ~700 kW·h and ~230 kW·h, respectively (Supporting Information). In the DMF+ETA case of 92% conversion rate, the mechanical-to-chemical energy conversion efficiency is estimated to be between 53% and 79.5% (see Supplementary discussion,

Supporting Information). Note that the energy cost for CO_2 purification is not considered in our calculations. An overall estimation based on the current price of electricity suggests that the operational cost of CO_2 capture and conversion using DMF+ETA is lower than any other state-of-the-art technologies.[25-29]

We also used lower concentrations of CO_2 (20% and 6%, diluted with N_2) and introduced 5% water into the reaction system to crudely simulate commonly encountered CO_2 sources such as flue gas or exhaust gas (see Figure S12, Table S2 and Supplementary discussion for details, Supporting Information). CO_2 conversion was observed in all cases and the small amount of water did not decrease the conversion rate. These results demonstrate the promising capability of our reaction system for low concentration CO_2 conversion without pre-purification.

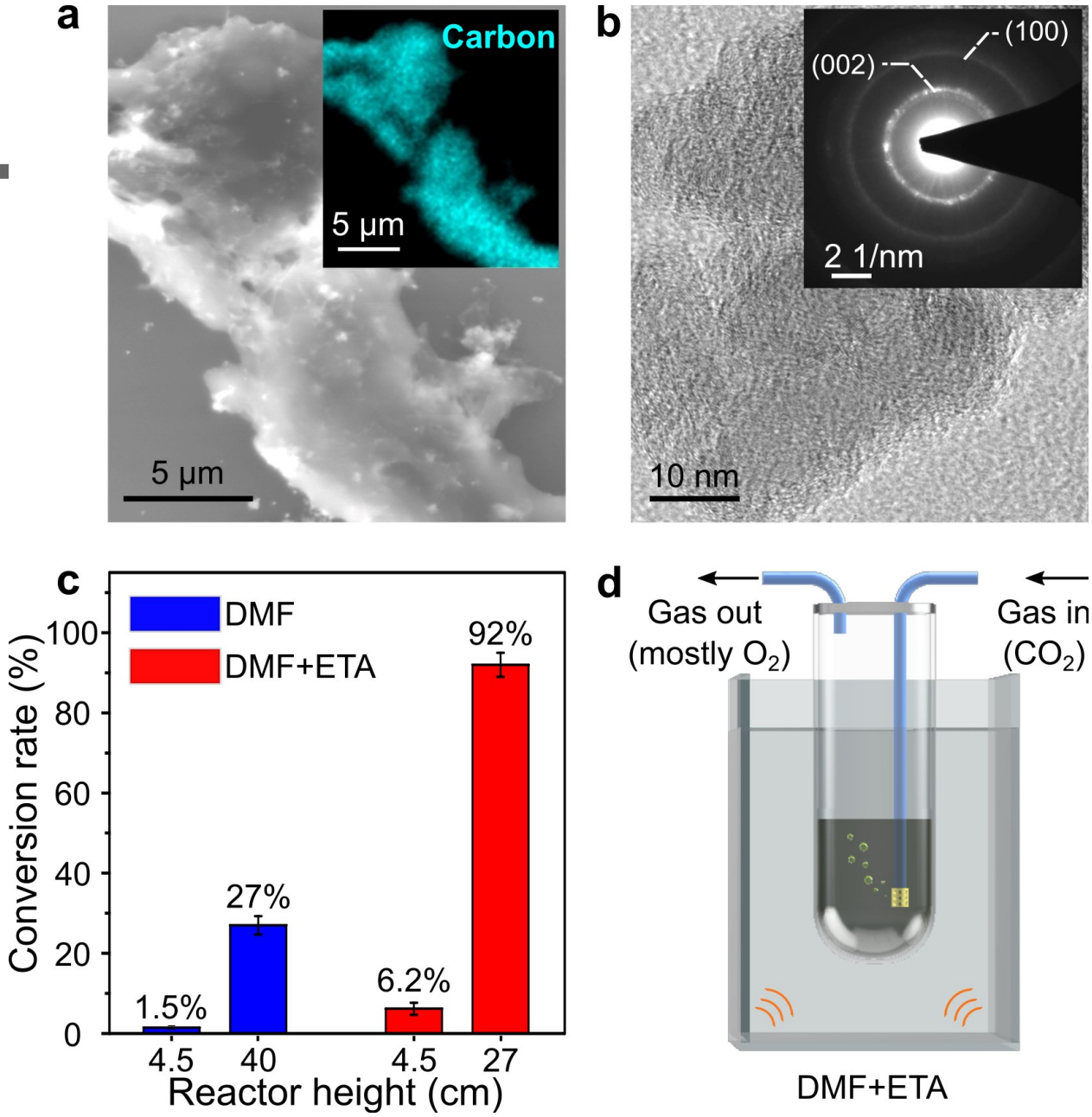

Figure 2. Characterisations of the carbonaceous products and the demonstration of the scalability of the technology. a) SEM and EDS images (inserted in a) of the carbonaceous materials. b) TEM and SAED (inserted in b) images of the separated carbonaceous products. c) Conversion efficiencies of CO_2 under different configurations showing the maximum efficiency of 92% for CO_2 capture and conversion in DMF+ETA case. d) Schematic representations of the scaled-up reactors for full CO_2 conversion for DMF+ETA reactors (refer to Supporting Information for the actual picture of the reactor).

2.4. Analysis of the suspensions

To elucidate how the functional materials are formed during the probe sonication stage, the reactions between Ga and silver salts were investigated by characterising the sonication products. Sonicating Ga with AgF (as an exemplar) forms an intermetallic phase $Ag_{0.72}Ga_{0.28}$ (**Figure 3**a) and GaF_3. The existence of metallic Ag (as $Ag_{0.72}Ga_{0.28}$) is confirmed by the Ag3d XPS peaks at 367.8 and 373.8 eV (Figure 3b).[30] The metallic fluorides can be verified by the F1s XPS peak at 684.3 eV (Figure 3c).[31]

The compositions and morphologies of the materials were investigated and correlated with the CO_2 reduction performance. As illustrated in Figure 3a, XRD patterns of Ga mixed with silver salts, which lead to CO_2 conversion (i.e., AgF, AgCl, AgBr, AgI and AgOTf), show the presence of $Ag_{0.72}Ga_{0.28}$ crystalline peaks. The control experiments show that Ag_2Ga particles (generated from the sonication of Ga-Ag alloy, Figure S13, Supporting Information) and Ag particle inclusions (using Ga/$AgNO_3$ as the precursors, Figure 3a,d) are inactive materials for CO_2 conversion. These results suggest that the formation of $Ag_{0.72}Ga_{0.28}$ is a prerequisite for CO_2 reduction. Interestingly, the $Ag_{0.72}Ga_{0.28}$ crystals, generated from different silver salts, show distinct morphologies (Figure 3e-i and Figure S14, Supporting Information) of particles (Figure 3e-g) or rods (Figure 3i for AgF) or a combination of both (Figure 3h for AgCl) together with the Ga spheres. The presence of only rod-shaped morphology (Figure 3i for AgF) is found to associate with an enhanced CO_2 catalytic capability. The Ga/AgF system, which generated the highest efficiency for CO_2 conversion, showed the rod-shaped $Ag_{0.72}Ga_{0.28}$, while $Ag_{0.72}Ga_{0.28}$ with non-rod morphology from other silver salts (or limited rod morphology for AgCl) exhibited limited catalytic abilities. The high-resolution TEM images, SAED pattern (Figure 3j,k) and the TEM-based EDS mapping (Figure 3l-n) further confirm the existence of the $Ag_{0.72}Ga_{0.28}$ rods and their growth direction along the [201] plane (Figure 3k). As shown in Figure

3o-q, the native oxide layer on the surface of the Ga droplets can be observed when dried for analysis. Furthermore, there were no obvious changes to the $Ag_{0.72}Ga_{0.28}$ structures after 5 hours of reaction according to both XRD (Figure S14x, Supporting Information).

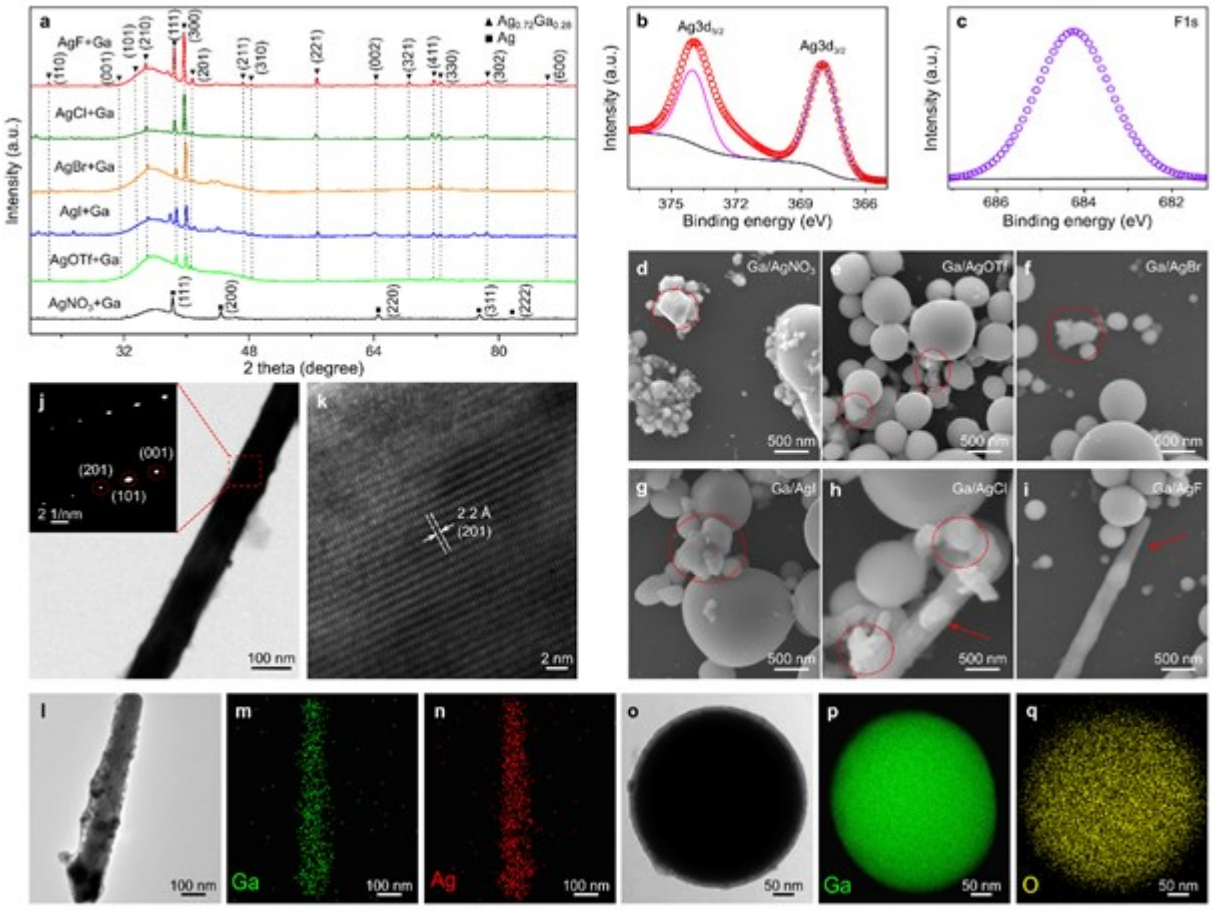

Figure 3. Characterisation of the functional materials. a) XRD patterns after probe sonication by employing different silver salts with Ga as the precursors. Except for $Ga/AgNO_3$, the other silver salts and Ga were converted into $Ag_{0.72}Ga_{0.28}$. b,c) XPS analysis of the state of silver and fluoride on the surface of the mixtures after probe sonication. d-i) SEM images of the materials after probe sonication when different silver salts were used as precursors as $Ga/AgNO_3$ (d), Ga/AgOTf (e), Ga/AgBr (f), Ga/AgI (g), Ga/AgCl (h), and Ga/AgF (i). $Ag_{0.72}Ga_{0.28}$ was found in the shape of rods only when AgF was used as the precursor, and some rods were also seen for the AgCl case, while $Ag_{0.72}Ga_{0.28}$ from other silver salts have non-rod morphologies. j,k) TEM and HRTEM of $Ag_{0.72}Ga_{0.28}$ nanorods with SAED images inserted in j. l-q) TEM and corresponding EDS images of $Ag_{0.72}Ga_{0.28}$ rods and Ga droplets.

The concentration of gallium and silver ions in solution during the reaction was measured by inductively coupled plasma mass spectrometry (ICP-MS) (Figure S15, Supporting Information). The ion concentrations fluctuated without showing any increasing or decreasing trend, indicating that the catalysts are not consumed, and that the system is stoichiometrically stable.

2.5. Reaction mechanism

Based on the configuration of the catalytic process, we can consider a scenario in which the interfacial charge of the Ga droplets is altered by the fast frictional contact of the $Ag_{0.72}Ga_{0.28}$ rods under sonication. The contact instantaneously generates an ultra-thin surface oxide on the Ga droplets,[32] which leads to a localized contact electrification of the oxidized site at the Ga/DMF interface as previously described. The formation of a closed loop, by the $Ag_{0.72}Ga_{0.28}$ rods, thereafter, initiates the CO_2 conversion. The presence of the triboelectric effect can be validated by proof-of-concept macro sized experiments that is illustrated in **Figure 4**a (see discussion in Supporting information). As can be seen, after the sharp ended electrode touches the surface of the liquid metal, immediately a large triboelectric voltage is produced (Figure 4b), which is different from the galvanic voltage of 0.88 V (Figure 4c). The formation of the oxide layer is seen in Figure 4d-g (refer to equation (1)). When the sharp electrode detaches from the surface, the surface oxide immediately disappears (Figure 4h), demonstrating the reversibility of the system (equation (1)). The equilibrated Ga ion concentration (Figure S15, Supporting Information) together with the rest of the mechanism discussions, which will be presented in the following section, also suggest that the localized Ga oxidation in nano size is reversible and Ga is not consumed during the process.

$$4\mathrm{Ga} + 3\mathrm{O_2} \rightleftharpoons 2\mathrm{Ga_2O_3} \quad (1)$$

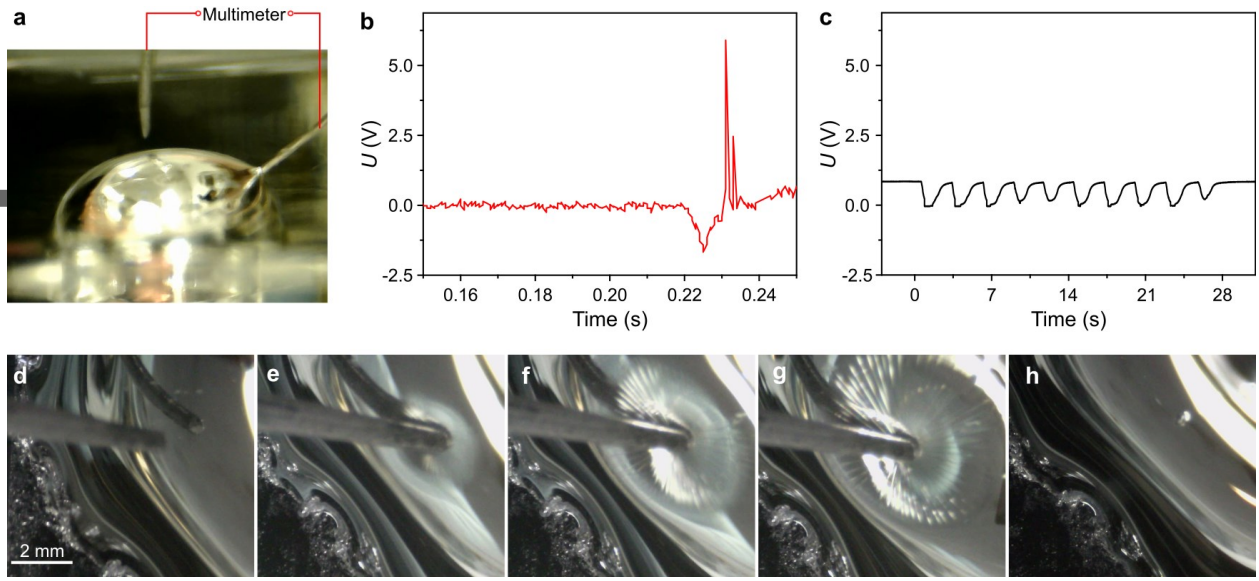

Figure 4. Voltage measurement between a Ga liquid droplet and a AgGa electrode and observation of the state of Ga surface upon the contact by a metallic needle. a) The set-up for measuring the voltage *U*, between the AgGa and Ga droplet in the DMF + ETA solution with the addition of HCl (0.1 M). b) The triboelectric voltage generated during the fast contact-detach process between the AgGa and Ga droplet measured at the input impedance of 25 MΩ. c) The measurements of the galvanic potential between the AgGa and Ga droplet when the AgGa was penetrated into the Ga droplets during 10 repeated cycles (measured at input impedance of 1 MΩ). A large triboelectric voltage of about 5.5 V was measured between the two electrodes during their instant contact-detach, which is much higher than the galvanic potential presented in c. d-h) The oxidation of the Ga droplet surface upon the contact-detach of a metallic needle in DMF+ETA solution with the addition of HCl (0.1 M).

The CO_2 reduction in our system is completed through a reversible Ga-Ga^+ cycle. Cyclic voltammetry was conducted to provide an insight into the catalytic mechanism of the $Ag_{0.72}Ga_{0.28}$ rods *via* the suggested route. The results showed that, for the working electrode containing Ga droplets and $Ag_{0.72}Ga_{0.28}$ rods as the co-contributors, Ga is oxidized to Ga^+ at 0.18 V and then reduced to elemental gallium at -0.31 V (**Figure 5**a).[33] Considering that the triboelectric process generates time-dependent voltages of several volts, the carbonaceous sheets are rapidly produced on the surface of liquid metals as we have previously demonstrated.[34] We also note that Ga^+ reduction was not observed when either Ga droplets (Figure 5b), $Ag_{0.72}Ga_{0.28}$ rods (Figure 5c) or Ga droplets with non-

rod morphology $Ag_{0.72}Ga_{0.28}$ were used as the working electrode (Figure S17, Supporting Information), showing the importance of the long rods for the cyclic reaction.

To investigate the reaction mechanism, we performed a detailed assessment of the reaction intermediates and the by-products generated during CO_2 reduction. The overall reaction process in DMF is described by chemical reaction equations (2-7). The equations are separated into 'liquid metal components' reactions (equations (2-5)) and 'solid components' reactions (equations (6,7)). For the description of the liquid metal component reactions, a series of characterisations were conducted. Nuclear magnetic resonance (NMR) analysis showed that the solvent DMF was not involved in the reaction (Figure S18a, Supporting Information). The CO_2 reduction is realised *via* the voltage provided by the nano triboelectrochemical process on the surface of Ga liquid droplets that turn Ga into Ga^+, while CO_2 is activated into the $CO_2^{\bullet-}$ radical (equation (2), Figure 5e-g, see Figure S19, S20 and Supplementary discussion, Supporting Information). The existence of the $CO_2^{\bullet-}$ radical during the reaction is demonstrated by electron paramagnetic resonance (EPR), which uses 5,5-dimethyl-1-pyrroline N-oxide (DMPO) as a radical trapping agent to form DMPO-$CO_2^{\bullet-}$ adduct for spectroscopic analysis (Figure 5e, see Methods).[35] The CO_2 to $CO_2^{\bullet-}$ process is followed by the generation of the intermediates CO and O^{2-} radicals (equation (3), see Supplementary discussion about the O^{2-} radical, Supporting Information).[36] The former is further converted to carbonaceous materials on the liquid metal surface (equation (4) which is the optimum case and it can be altered according to the C to O ratio in the obtained carbonaceous solid). The equations are as follows:

$$Ga + CO_2 \rightarrow Ga^+ + CO_2^{\cdot-} \quad (2)$$

$$CO_2^{\cdot-} + Ga \rightarrow CO + Ga^+ + O^{2-} \quad (3)$$

$$CO + 2Ga \rightarrow C + 2Ga^+ + O^{2-} \quad (4)$$

$$2O^{2-} \rightarrow O_2 + 4e^- \quad (5)$$

The description of the 'solid components' reactions is as follows. According to the cyclic voltammetry results, the oxidized Ga^+ can be reduced to elemental Ga by receiving an electron from the $Ag_{0.72}Ga_{0.28}$ and the $Ag_{0.72}Ga_{0.28}$ turns into $Ag_{0.72}Ga_{0.28}^+$ (equation (6)). The catalytic cycle is closed by the electrons provided from the O^{2-} to O_2 (equation (5)) to reduce $Ag_{0.72}Ga_{0.28}^+$ back to $Ag_{0.72}Ga_{0.28}$ (equation (7)), where the existence of O_2 can be confirmed through GC (Figure S5 and Table S1, Supporting Information). Altogether, the $Ag_{0.72}Ga_{0.28}$ rods remain intact (Figure S10, Supporting Information) during the process and the Ga-Ga^+ cycle plays a crucial role as evidenced by X-ray absorption near edge structure (XANES) spectroscopy (Figure 5f),[37, 38] XPS (Figure 5g), and electrochemical analyses (Figure 5a-c).

$$4Ga^+ + 4Ag_{0.72}Ga_{0.28} \rightarrow 4Ga + 4Ag_{0.72}Ga_{0.28}^+ \quad (6)$$

$$4Ag_{0.72}Ga_{0.28}^+ + 4e^- \rightarrow 4Ag_{0.72}Ga_{0.28} \quad (7)$$

The triboelectric potential generated during the oxide formation and reversible Ga to Ga^+ conversion process drive the CO_2 activation and conversion. They also guarantee the reversibility of the system. For clarity, a closed loop equivalent circuit formed by Ga droplet, the reversible oxide layer and $Ag_{0.72}Ga_{0.28}$ rod is presented in Figure S21 Supporting Information that describes how the electrochemical system operates. The catalytic cycle of CO_2 reduction at the interface of Ga droplets is illustrated in Figure 5d. This catalytic mechanism also aligns with the DMF+ETA case, and the extra by-products are produced due to the presence of ETA that promotes the process towards CO production according to equation (3) (Figure S5 and Figure S18b, Supporting Information).[39] Further experiments with ^{13}C labelling (Figure S22, Supporting Information),[40] NMR (Figure S11, Supporting Information) and a control experiment of long-term N_2 bubbling only (Figure S9g, Supporting Information) were conducted to show that during the reaction the solvent remains intact and only CO_2 is the source of the observed products.

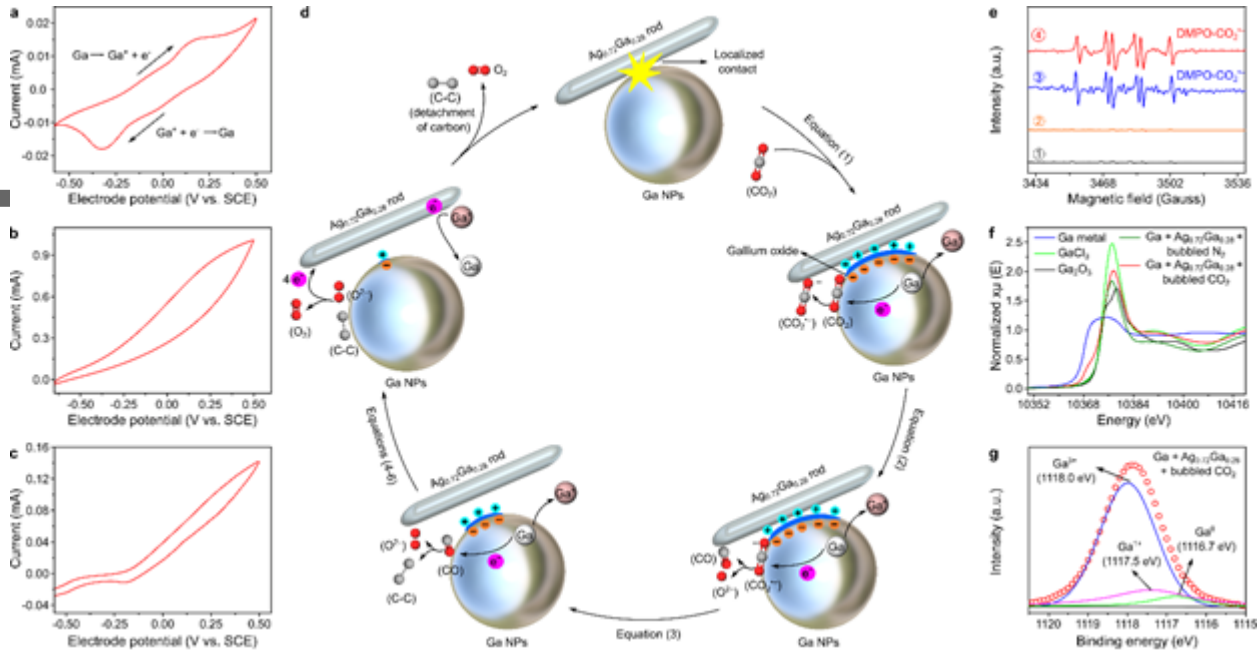

Figure 5. Reaction mechanism of CO_2 reduction. a) Cyclic voltammogram of the Ga^+-Ga cycle with Ga droplets and $Ag_{0.72}Ga_{0.28}$ rods as the working electrode. b,c) Cyclic voltammograms recorded with only Ga droplets and $Ag_{0.72}Ga_{0.28}$ rods as the working electrode. d) Proposed catalytic cycle for CO_2 reduction on the surface of Ga droplets with $Ag_{0.72}Ga_{0.28}$ rods working as the functional material. e) EPR spectra of the carbon dioxide radical ($CO_2^{\bullet-}$) addition to DMPO. (① Spectrum of DMPO added into the reaction solution for 30 min without bubbling CO_2. ② Spectrum of DMPO added into the CO_2 bubbled reaction solution for 30 min without energy input. ③ Spectrum of DMPO-$CO_2^{\bullet-}$ by ultraviolet photolysis of 100 mM $NaHCO_2$ and 100 μM H_2O_2 in the presence of 50 mM DMPO in Milli-Q water for 10 min, followed by the addition of photolytic 1.0 mL solution into 20 mL DMF for EPR analysis. ④ Spectrum of DMPO-$CO_2^{\bullet-}$ with DMPO added into the reaction solution for 30 min when CO_2 reduction is proceeding). f) XANES spectra of the reaction system containing Ga droplets and $Ag_{0.72}Ga_{0.28}$ rods with bubbling of CO_2 and N_2, and the reference spectra for Ga metal, $GaCl_3$ and Ga_2O_3. g) XPS showing the Ga 2p spectrum of Ga droplets and $Ag_{0.72}Ga_{0.28}$ rods after CO_2 conversion using Ga and AgF as the precursors. The XANES, XPS and electrochemical analyses further prove the accuracy of equations (1) to (6). See Supporting Information for further discussion.

Since the reaction is activated by the triboelectric potential, other forms of mechanical stimuli can also be applied, and the system can be readily scaled up. As a demonstration, we further validate our strategy by coupling an overhead stirrer to a 50 mL reactor. We found that CO_2 conversion continuously takes place in a stable manner when the stirring speed exceeds a threshold of 200 rpm (at room temperature, Figure S23a, Supporting Information) and the conversion efficiency increases

along with the increase of the stirring speed (equivalently, the mechanical energy input) (Table S1 and Figure S23b,c, Supporting Information). The input energy and its frequency (equivalently, rotation speed during overhead stirring) were found to affect the CO_2 conversion rate as well as the structure/stoichiometry of the produced carbonaceous materials (Figure S23 and Supplementary discussion, Supporting Information).

3. Conclusion

In conclusion, we demonstrated a promising mechanical energy-induced CO_2 conversion method which operates solely with mechanical stimuli. The catalytic process was found to be mechanically enabled by co-contributors containing liquid metal Ga droplets and resilient intermetallic $Ag_{0.72}Ga_{0.28}$ structures. We demonstrated the crucial roles of the composition and morphology of the functional materials, as well as the importance of precursor selection for triboelectrochemical CO_2 conversion. The obtained CO_2 capture and conversion efficiency was 92% for a reactor with a height as small as 27 cm at the input CO_2 flow rate of ~8 sccm. As one of the by-products, O_2 acts as an essential part during the CO_2 conversion process. The oxygen tolerance of our system can be an advantage when compared to other CO_2 conversion techniques which require oxygen-free environments.

The prospects of further exploring the proposed system are extensive. This methodology can be extended for large-scale systems and long-term operation by employing different forms of mechanical energies. This methodology with its remarkable capabilities provides promising prospects for future practical deployment of CO_2 conversion technologies. The carbonaceous materials presented here are produced at low costs. These by-products can be used as construction materials, fillers for various composites, supercapacitor ingredients, adsorbents for filtering, and catalyst support. Altogether, the novel concept provided by this new system offers a platform to fundamentally impact the future of carbon capture technologies and relevant industries.

4. Methods

Materials: Gallium (Ga, ingot, purity: 99.99%) was purchased from Rotometals, USA, and silver powder (purity: 99.9%) was obtained from Sigma-Aldrich. All the salts, including AgF, AgCl, AgBr, AgI, AgOTf, $AgNO_3$, KCl, NaCl and $NaHCO_2$, were obtained from Sigma-Aldrich with a purity of 99.5%. The solvents DMF (purity: 99.8%, boiling point: 153 °C), ETA (purity: ~ 98%, boiling point: 170 °C) and HCl (33 wt% in water) were acquired from Chem-Supply Pty Ltd. HNO_3 (acidimetric: ≥ 65.0%), DMPO (purity: 99.9%) and H_2O_2 (30 wt% in water) were purchased from Sigma-Aldrich. Milli-Q water was used throughout the experiments for sample preparation and reaction.

Preparation of functional materials: (1) Sliver salts as precursors: During a typical co-contributor preparation process (using AgF as an example), Ga (7.0 g) was first added into a glass vial which is pre-filled with 5.0 mL DMF solution, followed by adding HCl solution to give a final 0.10 M to remove the surface oxide layer of Ga. AgF (1.0 g) was then added to the mixture as the precursor.

(2) Ag (150 nm particle size) as precursors: For the preparation of Ag-Ga alloy, the silver powder was added to Ga (7.0 g) in concentrations of 2.0 wt% and 5.0 wt%, respectively. The mixtures were ground using a mortar and pestle inside a N_2-filled glove box to minimize oxidation of the liquid metal.[16] The grinding process, typically lasts 40 min, was stop until the sample showed a smooth and reflective appearance.

(3) Probe sonication procedures: The mixture from step (1) or step (2) was sonicated with a probe sonicator (VC 750, Sonics & Materials) under the protection of N_2. The sonication amplitude was set to 55%, corresponding to an ultrasonic power input of ~410 W. The sonicator was paused for 1 s after each 9 s sonication and the total sonication time was 30 min.

CO_2 conversion experiment: (1) Bath sonication as the energy source: After the preparation of functional material, CO_2 was continuously bubbled into the reactor through a diffuser and the flow rate of CO_2 gas (10 sccm) was controlled using a gas mass flow controller (MKS, GE50A). Bath sonication (FREQ 50Hz, Unisonics) was employed as the mechanical energy source to trigger CO_2 conversion. The temperature of the reaction solution was kept around 40 °C during the 5 hours reaction for the referencing reactions and longer hours for the experiments focused on longevity of the reaction. During the sonication, the system was switched off every 90 min for one minute.

(2) Overhead stirrer as the energy source: When CO_2 was bubbled into the reactor through a diffuser at the same rate of 10 sccm, an overhead stirrer (DLS Digital Overhead Stirrer, 120 W) was utilized as the mechanical energy source. Different rotation speeds, including 200, 300, 400, 500 and 1000 rpm, were applied for initiating the CO_2 conversion. The experiment was performed at room temperature for 24 hours.

Sample characterisations: Raman spectra were collected via a Raman spectrometer (Via Raman microscope, Renishaw) utilizing the 532 nm laser source. XPS was performed on a Thermo Scientific K-alpha X-ray spectrometer. The carbon product was studied using micro-FTIR spectroscopy, on a PerkinElmer Spectrum 100 FTIR Spectrometer which is coupled to a Spotlight 400 FTIR Imaging System with stage controller. The morphology and structure of materials were imaged by SEM (JEOL JSM-IT-500 HR). The TEM and SAED characterisations were performed on a Phillips CM200 TEM system. Both the SEM and the TEM systems are coupled with an EDS detector for elemental and compositional analysis. The crystalline phases of the samples were characterised by XRD (Philips X'Pert Pro MPD, λ = 1.54 Å, Cu-Kα radiation). The TGA for carbonaceous material quantification was performed on a Thermogravimetric Analyzer TGA Q5000 IR. ICP-MS was performed on NexION 2000 B ICP Mass Spectrometer to determine the concentration of gallium and silver ions. EPR experiments for the detection of the $CO_2^{\bullet-}$ radicals were conducted on a Bruker EMX X-Band ESR Spectrometer

(Bohr). NMR experiments were performed to investigate the liquid species in the solution, which was performed by using Bruker Avance III 600 MHz Cryo NMR (Ernst).

Preparation and analysis of TGA samples: The carbonaceous materials for the TGA experiments were separated by centrifugation. After a specific reaction time (*T*, h), the homogeneous mixture from the reactor (2.0 mL) was added into a centrifuge tube followed by centrifuging at a speed of 10000 rpm for 10 min. During this process, the suspended solid materials were separated into different layers. Most of the metallic catalysts deposit at the bottom of the tube due to their high density, in comparison to the carbonaceous materials which remains suspended in the top layer. The centrifugation process was repeated three times and each time the carbon-containing top layer was collected. The collected materials (sample volume V_{TGA} = 2.0 mL solution during certain reaction time *T* (h)) were then dried (110 °C) to remove DMF from the samples before the TGA experiments. During the TGA experiments, the heating rate was set to 10 °C/min and the upper temperature limit was fixed at 800 °C.

ICP-MS samples: During the process of CO_2 reduction, 1.0 mL reaction mixture was taken as a sample every hour and then we centrifuged the sample for 15 min at 10000 rpm until all the suspended materials deposit at the bottom of the tube. Then, we took 0.20 mL clear solution from the top of the sample and heated it on the hot plate until it was completely dried. Thereafter, 0.20 mL of nitric acid was added to dissolve the residue for ICP-MS.

Cyclic voltammetry experiments: Cyclic voltammetry experiments were conducted to investigate the roles of the $Ag_{0.72}Ga_{0.28}$ rods during the CO_2 reduction. Ga droplets and $Ag_{0.72}Ga_{0.28}$ rods were obtained from the Ga and AgF precursors. Then, we painted the Ga/$Ag_{0.72}Ga_{0.28}$ ($Ag_{0.72}Ga_{0.28}$ in the shape of a rod) on fluorine doped tin oxide (FTO) and baked it until the material dried and immobilised on the FTO as the working electrode. A calomel reference electrode and a gold counter electrode were used to set up a three-electrode configuration. DMF+ETA solution containing 0.10 M

HCl was utilized as the electrolyte to keep the condition consistent to the reaction situation. As a comparison, Ga droplets, concentrated $Ag_{0.72}Ga_{0.28}$ rods and Ga/$Ag_{0.72}Ga_{0.28}$ ($Ag_{0.72}Ga_{0.28}$ with non-rod morphology, using Ga/AgI) were painted on FTO as the working electrode respectively and all other parameters were kept identical.

EPR experiments: To provide mechanistic insights, EPR experiments were conducted to confirm the existence of the activated CO_2. DMPO is known as a standard $CO_2^{\bullet-}$ radical captor and the combination of DMPO with the $CO_2^{\bullet-}$ radical shows characteristic signals.[35, 41] During the experiments, 20 mg DMPO was added and dissolved into 5.0 mL Milli-Q water and then 1.0 mL DMPO solution was further added into the reaction system. After bubbling CO_2 into the solution in the presence of bath sonication for 30 min, 1.0 mL reaction solution was centrifuged to remove all the suspended materials for EPR measurement. As a control, 1.0 mL DMPO solution was added into the reaction system in the process of bath sonication without bubbling CO_2.

To verify that the EPR signal obtained from our reaction system was due to the formation of $CO_2^{\bullet-}$, an independent reaction involving $CO_2^{\bullet-}$ formation is further conducted. It is well established that the $CO_2^{\bullet-}$ radical can be generated from $NaHCO_2$ and H_2O_2 under the irradiation of ultraviolet light.[35] $NaHCO_2$ and 30% H_2O_2 were dissolved in 5.0 mL Milli-Q water in the concentration of 100 mM and 100 µM, respectively, with the DMPO concentration being 50 mM. After irradiation with ultraviolet light for 10 min, we mixed 1.0 mL photolytic solution with 20 mL DMF solution for EPR analysis to keep the condition consistent with the conditions of our CO_2 conversion reaction. By comparison, the EPR spectra from the reaction system and photolytic solution were in good agreement, thereby validating the existence of $CO_2^{\bullet-}$ radical during our CO_2 conversion reaction (Figure 5c).

XANES samples and experiments: The XANES experiments were performed at the XAS Beamline at the Australian Synchrotron, ANSTO Melbourne. Ga metal and Ga metal + $Ag_{0.72}Ga_{0.28}$ samples in DMF

+ ETA + 25% glycerol (by volume, glycerol was required for liquid samples), bubbled with CO_2 and N_2, with and without Ga^+ stabilizer (18-Crown-6), were tested. In addition, standards of pure gallium (pressed between kapton tape), Ga_2O_3 (prepared as a powder pellet), and $GaCl_3$ were measured as references for Ga^0 and Ga^{3+}. Nine samples (see Table S3, Supporting Information) were sonicated for 1 hour before being sealed into aluminium sample holders between layers of kapton tape. Sealed sample holders were immersed in liquid nitrogen to freeze then were stored on dry ice prior to analysis and were maintained at approximately 4 K in a helium atmosphere during analysis.

XAS spectra were recorded by measuring Ga-K fluorescence using a 100-element solid state HP-Ge detector (Canberra/Mirion, France). The excitation energy was selected using a Si(111) double crystal monochromator, which was calibrated at the Pt-L3 absorption edge using an inline Pt metal foil (first maximum of the first derivative at 11,564 eV). The X-ray beam was focussed at the sample position and slits were used to reduce the beam size to a $\approx$1 mm spot. Short, repeat XAS scans of Sample 3 were performed to determine that the materials were sufficiently impervious to X-ray exposure for at least several minutes, thus permitting adequate XAS analyses to be conducted for the purpose of this project. XANES scans were then collected with a count time of 2 seconds for each energy step in the pre-edge and XANES region, with 10 eV steps in the pre-edge region of the XAS spectra (10167 – 10347 eV), 0.25 eV steps in the XANES region (10347 – 10417 eV). In the EXAFS region spectra were collected, in steps of 0.035 k to a maximum of 10 k, with count time increasing linearly from 2 seconds up to 4 seconds at the end of the energy range. Multiple scans were collected for each sample. Data were pre-processed using Sakura (in-house program) and the Athena program for scan averaging, background subtraction and edge-height normalisation (Ravel and Newville, 2005). Periodically throughout the experiment, transmission scans were collected of the in-line Re foil.

Supporting Information

Supporting Information is available from the Wiley Online Library or from the author.

Acknowledgments

This work was supported by the Australian Research Council (ARC) Laureate Fellowship grant (FL180100053), the ARC Center of Excellence FLEET (CE170100039) and Chevron. The authors would like to thank Dr. Yin Yao, Dr. Sean Lim of the Electron Microscope Unit within the Mark Wainwright Analytical Centre at UNSW Sydney, and Dr. Donald Thomas of the Spectroscopy Laboratory and the Nuclear Magnetic Resonance Facility for their technical assistance.

Competing interests

The authors declare no competing interests.

References

[1] S. Mukherjee, N. Sikdar, D. O'Nolan, D. M. Franz, V. Gascón, A. Kumar, N. Kumar, H. S. Scott, D. G. Madden, P. E. Kruger, B. Space, M. J. Zaworotko, *Sci. Adv.* **2019**, 5, eaax9171.

[2] F. P. García de Arquer, C.-T. Dinh, A. Ozden, J. Wicks, C. McCallum, A. R. Kirmani, D.-H. Nam, C. Gabardo, A. Seifitokaldani, X. Wang, Y. C. Li, F. Li, J. Edwards, L. J. Richter, S. J. Thorpe, D. Sinton, E. H. Sargent, *Science* **2020**, 367, 661.

[3] S. Gao, Y. Lin, X. Jiao, Y. Sun, Q. Luo, W. Zhang, D. Li, J. Yang, Y. Xie, *Nature* **2016**, 529, 68.

[4] C. W. Li, J. Ciston, M. W. Kanan, *Nature* **2014**, 508, 504.

[5] X. Li, Y. Sun, J. Xu, Y. Shao, J. Wu, X. Xu, Y. Pan, H. Ju, J. Zhu, Y. Xie, *Nat. Energy* **2019**, 4, 690.

[6] Y. Wu, Z. Jiang, X. Lu, Y. Liang, H. Wang, *Nature* **2019**, 575, 639.

[7] S. Nahar, M. F. M. Zain, A. A. H. Kadhum, H. A. Hasan, M. R. Hasan, *Materials (Basel)* **2017**, 10.

[8] X. Liu, J. Xiao, H. Peng, X. Hong, K. Chan, J. K. Norskov, *Nat. Commun.* **2017**, 8, 15438.

[9] M. A. Stuart, W. T. Huck, J. Genzer, M. Muller, C. Ober, M. Stamm, G. B. Sukhorukov, I. Szleifer, V. V. Tsukruk, M. Urban, F. Winnik, S. Zauscher, I. Luzinov, S. Minko, *Nat. Mater.* **2010**, 9, 101.

[10] T. Gan, S. Handschuh-Wang, W. Shang, J. Shen, L. Zhu, Q. Xiao, S. Hu, X. Zhou, *Macromol Rapid Commun.* **2019**, 40, e1900537.

[11] G.-F. Han, F. Li, Z.-W. Chen, C. Coppex, S.-J. Kim, H.-J. Noh, Z. Fu, Y. Lu, C. V. Singh, S. Siahrostami, Q. Jiang, J.-B. Baek, *Nat. Nanotechnol.* **2021**, 16, 325.

[12] M. Sun, Q. Lu, Z. L. Wang, B. Huang, *Nat. Commun.* **2021**, 12, 1752.

[13] M. Asadi, B. Kumar, A. Behranginia, B. A. Rosen, A. Baskin, N. Repnin, D. Pisasale, P. Phillips, W. Zhu, R. Haasch, R. F. Klie, P. Kral, J. Abiade, A. Salehi-Khojin, *Nat. Commun.* **2014**, 5, 4470.

[14] H. Li, P. Wen, D. S. Itanze, Z. D. Hood, X. Ma, M. Kim, S. Adhikari, C. Lu, C. Dun, M. Chi, Y. Qiu, S. M. Geyer, *Nat. Commun.* **2019**, 10, 5724.

[15] C. G. Morales-Guio, E. R. Cave, S. A. Nitopi, J. T. Feaster, L. Wang, K. P. Kuhl, A. Jackson, N. C. Johnson, D. N. Abram, T. Hatsukade, C. Hahn, T. F. Jaramillo, *Nat. Catal.* **2018**, 1, 764.

[16] D. Esrafilzadeh, A. Zavabeti, R. Jalili, P. Atkin, J. Choi, B. J. Carey, R. Brkljaca, A. P. O'Mullane, M. D. Dickey, D. L. Officer, D. R. MacFarlane, T. Daeneke, K. Kalantar-Zadeh, *Nat. Commun.* **2019**, 10, 865.

[17] D. A. Torelli, S. A. Francis, J. C. Crompton, A. Javier, J. R. Thompson, B. S. Brunschwig, M. P. Soriaga, N. S. Lewis, *ACS Catal.* **2016**, 6, 2100.

[18] M. Losurdo, A. Suvorova, S. Rubanov, K. Hingerl, A. S. Brown, *Nat. Mater.* **2016**, 15, 995.

[19] E. J. Markvicka, M. D. Bartlett, X. Huang, C. Majidi, *Nat. Mater.* **2018**, 17, 618.

[20] B. Qin, U. Schneider, *J. Am. Chem. Soc.* **2016**, 138, 13119.

[21] M. Jitaru, *J. Univ. Chem. Technol. Metallurgy* **2007**, 42, 333.

[22] T. Daeneke, K. Khoshmanesh, N. Mahmood, I. A. de Castro, D. Esrafilzadeh, S. J. Barrow, M. D. Dickey, K. Kalantar-Zadeh, *Chem. Soc. Rev.* **2018**, 47, 4073.

[23] J.-Y. Park, S. J. Yoon, H. Lee, *Environ. Sci. Technol.* **2003**, 37, 1670.

[24] L. Chen, Z. Xu, J. Li, B. Zhou, M. Shan, Y. Li, L. Liu, B. Li, J. Niu, *RSC Adv.* **2014**, 4, 1025.

[25] K. Z. House, A. C. Baclig, M. Ranjan, E. A. van Nierop, J. Wilcox, H. J. Herzog, *Proc. Natl. Acad. Sci. U. S. A.* **2011**, 108, 20428.

[26] A. Kätelhön, R. Meys, S. Deutz, S. Suh, A. Bardow, *Natl. Acad. Sci. U. S. A.* **2019**, 116, 11187.

[27] D. W. Keith, G. Holmes, D. St. Angelo, K. Heidel, *Joule* **2018**, 2, 1573.

[28] R. Sen, A. Goeppert, S. Kar, G. K. S. Prakash, *J. Am. Chem. Soc.* **2020**, 142, 4544.

[29] R.-P. Ye, J. Ding, W. Gong, M. D. Argyle, Q. Zhong, Y. Wang, C. K. Russell, Z. Xu, A. G. Russell, Q. Li, M. Fan, Y.-G. Yao, *Nat. Commun.* **2019**, 10, 5698.

[30] J. Zhang, Y. Li, Y. Zhang, M. Chen, L. Wang, C. Zhang, H. He, *Sci. Rep.* **2015**, 5, 12950.

[31] Y. Li, M. Bettge, J. Bareño, S. E. Trask, D. P. Abraham, *J. Electrochem. Soc.* **2015**, 162, A7049.

[32] J. Tang, S. Lambie, N. Meftahi, A. J. Christofferson, J. Yang, M. B. Ghasemian, J. Han, F.-M. Allioux, M. A. Rahim, M. Mayyas, T. Daeneke, C. F. McConville, K. G. Steenbergen, R. B. Kaner, S. P. Russo, N. Gaston, K. Kalantar-Zadeh, *Nat. Nanotechnol.* **2021**, 16, 431.

[33] A. J. Bard, R. Parsons, J. Jordan, *Standard Potentials in Aqueous Solutions*, IUPAC, New York, USA 1985.

[34] M. Mayyas, H. Li, P. Kumar, M. B. Ghasemian, J. Yang, Y. Wang, D. J. Lawes, J. Han, M. G. Saborio, J. Tang, R. Jalili, S. H. Lee, W. K. Seong, S. P. Russo, D. Esrafilzadeh, T. Daeneke, R. B. Kaner, R. S. Ruoff, K. Kalantar-Zadeh, *Adv. Mater.* **2020**, 2001997.

[35] F. A. Villamena, E. J. Locigno, A. Rockenbauer, C. M. Hadad, J. L. Zweier, *J. Phys. Chem. A* **2006**, 110, 13253.

[36] H. V. Ijije, R. C. Lawrence, G. Z. Chen, *RSC Adv.* **2014**, 4, 35808.

[37] G. D. Meitzner, E. Iglesia, J. E. Baumgartner, E. S. Huang, *J. Catal.* **1993**, 140, 209.

[38] E. J. M. Hensen, M. García-Sánchez, N. Rane, P. C. M. M. Magusin, P.-H. Liu, K.-J. Chao, R. A. van Santen, *Catal. Lett.* **2005**, 101, 79.

[39] S. Zhang, P. Kang, S. Ubnoske, M. K. Brennaman, N. Song, R. L. House, J. T. Glass, T. J. Meyer, *J. Am. Chem. Soc.* **2014**, 136, 7845.

[40] R. Keiner, T. Frosch, T. Massad, S. Trumbore, J. Popp, *Analyst* **2014**, 139, 3879.

[41] Z. Barbieriková, D. Dvoranová, V. Brezová, *Catal. Today* **2018**, 313, 106.

With mechanical energy as the stimuli, CO_2 is converted into solid carbon and O_2 in a liquid metal-based reaction system. Using the synergism of Ga nano-droplets and Ag-Ga nano-rods, CO_2 conversion proceeds through the triboelectrochemical reaction on Ga, while the Ag-Ga rods ensure the system's sustainability. This is achieved at a remarkably low energy consumption and high efficiency.

Junma Tang, Jianbo Tang*, Mohannad Mayyas, Mohammad B. Ghasemian, Jing Sun, Md Arifur Rahim, Jiong Yang, Jialuo Han, Douglas J. Lawes, Rouhollah Jalili, Torben Daeneke, Zhenbang Cao, Claudia A. Echeverria, Francois-Marie Allioux, Ali Zavabeti, Jessica Hamilton, Valerie Mitchell, Anthony P. O'Mullane, Richard B. Kaner, Dorna Esrafilzadeh*, Michael D. Dickey, Kourosh Kalantar-Zadeh*

Liquid metal-enabled mechanical energy-induced CO_2 conversion

ToC figure